ORCA – Online Research @ Cardiff

Multi-temperature mapping of dust structures throughout the Galactic Plane using the PPMAP tool with Herschel Hi-GAL data

K. A. Marsh[1*], A. P. Whitworth[1], O. Lomax[1], S. E. Ragan[1], U. Becciani[2],
L. Cambrésy[3], A. Di Giorgio[4], D. Eden[5], D. Elia[4], P. Kacsuk[6], S. Molinari[4],
P. Palmeirim[7], S. Pezzuto[4], N. Schneider[8,9], E. Sciacca[2], F. Vitello[2]

[1] *School of Physics and Astronomy, Cardiff University, Cardiff CF24 3AA, UK*
[2] *INAF - Astrophysical Observatory of Catania, Italy*
[3] *Observatoire astronomique de Strasbourg, Université de Strasbourg, CNRS, UMR 7550, 11 rue de lUniversité, F-67000 Strasbourg, France*
[4] *Istituto di Astrofisica e Planetologia Spaziali - INAF, Via Fosso del Cavaliere 100, I-00133 Roma Italy*
[5] *Astrophysics Research Institute, Liverpool John Moores University, IC2, Liverpool Science Park, 146 Brownlow Hill, Liverpool, L3 5RF, UK*
[6] *MTA Sztaki, 1111 Budapest, Kende u. 13-17, Hungary*
[7] *Laboratoire d'Astrophysique de Marseille, CNRS/INSU-Université de Provence, 13388 Marseille cedex 13, France*
[8] *Université Bordeaux, LAB, UMR 5804, 33270 Floirac, France*
[9] *CNRS, LAB, UMR 5804, 33270 Floirac, France*

7 July 2017

ABSTRACT
The multi-temperature column density mapping procedure, PPMAP, is designed to aid in the modelling of dusty structures by providing resolution-enhanced image cubes of differential column density as a function of dust temperature. We discuss its application to data from the Hi-GAL survey, consisting of continuum images from the *Herschel* Space Observatory in the wavelength range 70–500 μm. We briefly describe PPMAP and present some illustrative examples of the results. These include multi-temperature maps of the Galactic bubble/HII region W5-E, the temperature decomposition of molecular cloud column density probability distribution functions, and the global variation of mean dust temperature as a function of Galactocentric distance. Amongst our findings are: (i) a strong localised temperature gradient in W5-E in a direction orthogonal to that towards the ionising star, thereby suggesting an alternate heating source and providing possible guidance for models of the formation of the bubble complex, and (ii) the overall radial profile of dust temperature in the Galaxy shows a monotonic decrease, broadly consistent both with models of the interstellar radiation field and with previous estimates at lower resolution. However, it also reveals the existence of a central temperature plateau within ~ 6 kpc of the Galactic centre, outside of which is a pronounced steepening of the radial profile. This behaviour may reflect the greater proportion of molecular (as opposed to atomic) gas in the central region of the Galaxy. The complete set of PPMAP image cubes, covering the entire Galactic Plane, is publicly available online.

Key words: Galaxy: structure — ISM: clouds — submillimetre: ISM — techniques: high angular resolution — stars: formation — stars: protostars.

1 INTRODUCTION

Mapping dusty structures in the Galaxy can provide key information constraining the ecological cycle associated with star formation. The PPMAP procedure (Marsh et al. 2015)

* E-mail: Ken.Marsh@astro.cf.ac.uk

is designed to extract information from such maps in a way which takes full advantage of the observations and knowledge of the instrumental response. Here we demonstrate the capabilities of the method by applying it to data from the Hi-GAL survey, which used the *Herschel* Space Observatory to map dust continuum emission from the entire Galactic plane at far-infrared wavelengths (Molinari et al. 2010).

PPMAP represents a significant step beyond conventional approaches to column density mapping in which it is assumed that the dust temperature is uniform everywhere along the line of sight (see, for example, Könyves et al. 2010; Peretto et al. 2010; Bernard et al. 2010), and the observed images are smoothed to a common spatial resolution. In the case of *Herschel* data, this usually corresponds to the 36 arcsec resolution at 500 μm, although some of the structure at the 18 arcsec resolution of the 250 μm data can be restored via spatial filtering techniques (Palmeirim et al. 2013). In contrast, PPMAP adds a third dimension, i.e., dust temperature, to the mapping procedure and does not require smoothing of the input images since it takes full account of the point spread functions (PSFs) of the telescopes used. The latter aspect enables a spatial resolution of 12 arcsec to be obtained with Hi-GAL data. A full mathematical description of the procedure is given in Marsh et al. (2015) and the essential points are summarised in the next section. All of the Hi-GAL data have been processed by PPMAP, and the results are available online[1]. Here we present some preliminary results to illustrate the type of information that can be derived.

2 THE PPMAP ALGORITHM

The essential concept of PPMAP is the *point process*, whereby the system under study is represented by a set of points in a suitably defined state space. In the present context, the system is a dusty astrophysical structure such as a core, filament or molecular cloud. It is represented by a set of small building-block components each of unit column density and each of which is parametrised by three variables, namely the x, y angular position on the sky and dust temperature, $T_{\rm D}$. Given a set of observational images of dust emission at multiple wavelengths, assuming the dust to be optically thin, the algorithm uses a non-hierarchical Bayesian procedure to generate a density function representing the expectation number of components per unit volume of state space. Because of the way that a component is defined, this density function is equivalent to differential column density as a function of x, y, and $T_{\rm D}$.

The measurement model upon which the estimation is based is of the form:

$$\mathbf{d} = \mathbf{A}\mathbf{\Gamma} + \mu. \qquad (1)$$

where $\mathbf{d}$ is the measurement vector whose $m^{\rm th}$ component represents the pixel value at location (X_m, Y_m) in the observed image at wavelength λ_m; $\mathbf{\Gamma}$ is a vector whose components represent the actual number of components in each cell of the state space; μ is the measurement noise assumed to be Gaussian; $\mathbf{A}$ is the system response matrix whose $mn^{\rm th}$ element expresses the response of the $m^{\rm th}$ measurement to an object which occupies the $n^{\rm th}$ cell in the state space, corresponding to spatial location (x_n, y_n) and dust temperature T_n; it is given by

$$A_{mn} = H_{\lambda_m}(X_m{-}x_n, Y_m{-}y_n) \, K_{\lambda_m}(T_n) B_{\lambda_m}(T_n) \, \kappa(\lambda_m) \, \Delta\Omega_m \,. \qquad (2)$$

in which $H_\lambda(x, y)$ is the convolution of the point spread function (PSF) at wavelength λ with the profile of an individual object; $K_\lambda(T)$ represents a colour correction[2]; $B_\lambda(T)$ is the Planck function; $\Delta\Omega_m$ is the solid angle subtended by the $m^{\rm th}$ pixel and $\kappa(\lambda)$ is the dust opacity law. For present purposes we adopt a simple power law of the form

$$\kappa(\lambda) = 0.1 \, {\rm cm}^2 \, {\rm g}^{-1} \left(\frac{\lambda}{300 \, \mu{\rm m}} \right)^{-\beta}. \qquad (3)$$

We use a power-law index, β, of 2, motivated by previous studies of Galactic dust emission at *Herschel* wavelengths which find that SEDs are fit well using this value (see (Sadavoy et al. 2012) and references therein). The reference opacity (0.1 cm^2 g^{-1} at 300 μm) is defined with respect to total mass (dust plus gas). Although observationally determined, it is consistent with a gas to dust ratio of 100 (Hildebrand 1983). It should be noted that there is evidence for variations in dust properties throughout the Galaxy and such variations impact the choices of both β and the reference opacity. For example, in the Galactic Centre region values of 1.2 and 0.042 cm^2 g^{-1}, respectively, may be more appropriate (Rathborne et al. 2015). Dust properties have also been found to differ between cool molecular clouds and warmer diffuse ISM (Cambresy et al. 2001; Paradis et al. 2011). While errors in the assumed reference opacity can be rectified by simple scaling of the output column densities, this is not true for the case of β variations. We have, however, investigated the effects of such variations and a quantitative example is presented in Section 4 below.

The *a priori* probability that a given cell in the state space is occupied by a source component is controlled by a "dilution" parameter, η, defined as the ratio of the number of source components to the total number of cells in the state space. The smaller the assumed value, the more the algorithm tries to fit the data with the least possible amount of source structure. The exact value is not critical, but the most appropriate value is one which results in a reduced chi squared value of order unity.

The principal inputs to PPMAP are a set of observed images of dust continuum emission, their associated PSFs, the assumed dust opacity law over the wavelength range of the observations, and a grid of temperature values at which the differential column density will be estimated. The input images could include not only *Herschel* data but also, where available, data from ground-based observatories, both single-dish and interferometric. The output is an image cube of differential column density of material (gas plus dust) per unit interval of dust temperature which, at each angular position, is expressed in units of hydrogen molecules per square centimetre per degree Kelvin. Also included in the output is a corresponding image cube of uncertainty values. Estima-

tion errors are Poisson-like, and increase in regions of high total column density.

As discussed by Marsh et al. (2015), the advantages over more conventional techniques for column density mapping are:

(i) increased spatial resolution resulting from the incorporation of PSF knowledge; all observational images are used at their native resolution and it is not necessary to smooth to a common resolution;

(ii) increased accuracy of peak column densities of compact features, due both to the resolution improvement and to taking proper account of temperature variations along the line of sight;

(iii) the temperature decomposition provides the potential ability to distinguish different physical phenomena superposed along the line of sight.

3 OBSERVATIONAL DATA AND ANALYSIS PROCEDURE

We have used PPMAP to produce image cubes for all of the Hi-GAL data, which consist of a set of *Herschel* PACS and SPIRE images at wavelengths of 70, 160, 250, 350, and 500 μm. The spatial resolution values of these data, i.e., the beam sizes at full width half maximum (FWHM), are approximately 8.5, 13.5, 18.2, 24.9, and 36.3 arcsec, respectively. Details of the calibration and map-making procedures are given by Elia et al. (2013). Briefly, calibration for both instruments was accomplished to Level 1 using routines in the *Herschel* Interactive Processing Environment (HIPE; Ott 2010), and subsequent map making utilised UNIMAP (Piazzo et al. 2015), which produced intensity maps in units of MJy/sr for each band. For the SPIRE bands, the extended-source flux calibration was used, based on band-averaged beam areas of 450, 795, and 1665 arcsec^2 at 250, 350, and 500 μm, respectively (Griffin et al. 2013). Calibration of the absolute background levels was achieved by applying a linear transform based on coefficients determined by comparing *Herschel* with *IRAS* and *Planck*, following Bernard et al. (2010). The resulting uncertainty in absolute flux density is $\sim 5\%$ for all bands.

The associated PSFs are based on the measured *Herschel* beam profiles (Poglitsch et al. 2010; Griffin et al. 2013). The adopted temperature grid consists of 12 temperatures equally spaced in $\log T_{\mathrm{D}}$ between 8 K and 50 K. It is designed to cover the expected range of temperatures to be encountered, based on an assessment of the observed spectral energy distributions (SEDs). The actual number of temperature values is guided by the effective temperature resolution, i.e., there should be a sufficient number of temperature values to ensure that the true temperature of a given source can be approximated by at least one of the available temperatures. The only penalty for using too many temperatures is that computational effort increases proportionately. In this sense, the selection of the temperature sampling interval is analogous to that of the spatial sampling interval. The 12 chosen temperatures represent discrete samples along the temperature axis—no averaging is done between samples. However, in order to approximate the continuous function representing the true temperature variation, the samples may be regarded as the midpoints of

a set of finite intervals, the ith of which can be expressed as $[(T_{i-1}+T_i)/2, (T_i+T_{i+1})/2]$.

The output spatial sampling interval for the present analysis is 6 arcsec per pixel, and the spatial resolution of the output maps is ~ 12 arcsec. The latter represents the Nyquist limit for the quoted sampling interval and corresponds to the minimum separation for which two adjacent point sources can be distinguished, even if the output image contains isolated peaks of smaller FWHM. It corresponds to a range of physical scales ~ 0.06–0.6 pc for the estimated range of distances, 1–10 kpc, involved in the Hi-GAL survey.

Regarding the dilution parameter, η, we used a value 10.0 for the majority of tiles. This value corresponds to a situation in which multiple components may occupy a given cell. The exact value, however, is not critical, and some improvement in resolution was obtained in a few cases by reducing it to 0.3. Those cases involved the tiles centred at nominal longitudes, ℓ, of 158°, 176°, 180°, 224°, 248°, and 316°. The effect, on the results, of the choice of η and other parameters is discussed below, using the $\ell = 17°$ tile as an example.

4 THE VIALACTEA DATABASE: ILLUSTRATIVE RESULTS

All 163 tiles of the Hi-GAL survey have been processed with PPMAP. Each tile covers a $2.4° \times 2.4°$ field and the complete set spans the entire Galactic plane. The results, now publicly available via the website indicated in footnote 1, consist of:

(i) a total of 163 image cubes of differential column density with 6 arcsec spatial pixels and 12 values along the temperature axis, covering the range 8–50 K in dust temperature;

(ii) corresponding image cubes of the uncertainties;

(iii) 2D maps of total column density and density-weighted mean dust temperature, derived from the image cubes.

Figs. 1–3 illustrate the full set of results for a representative tile centred at $\ell \simeq 17°$. This field contains the Eagle Nebula (M16), a site of massive star formation and the famous "pillars of creation" (Hester et al. 1996). Its far infrared properties, as observed by *Herschel*, are discussed by Hill et al. (2012). Fig. 1 shows the differential column density in all 12 temperature layers, and Fig. 2 shows the associated uncertainties. Clearly, the uncertainties are spatially quite uniform within each temperature bin, with no more than about a 50% variation across the field. This indicates that the errors are essentially background dominated, and the sensitivity varies as a function of temperature based on the form of the Planck function. The units of differential column density are "hydrogen molecules per square centimetre per bin," where "bin" refers to the temperature interval between adjacent midpoints as defined above. Fig. 3 shows the maps of integrated column density and mean (column density weighted) dust temperature, both of which were derived from the image cube itself.

Uncertainties in differential column density are obtained using the procedure specified in Marsh et al. (2015) and are based on measurement errors estimated from the sky background fluctuations in the individual observational
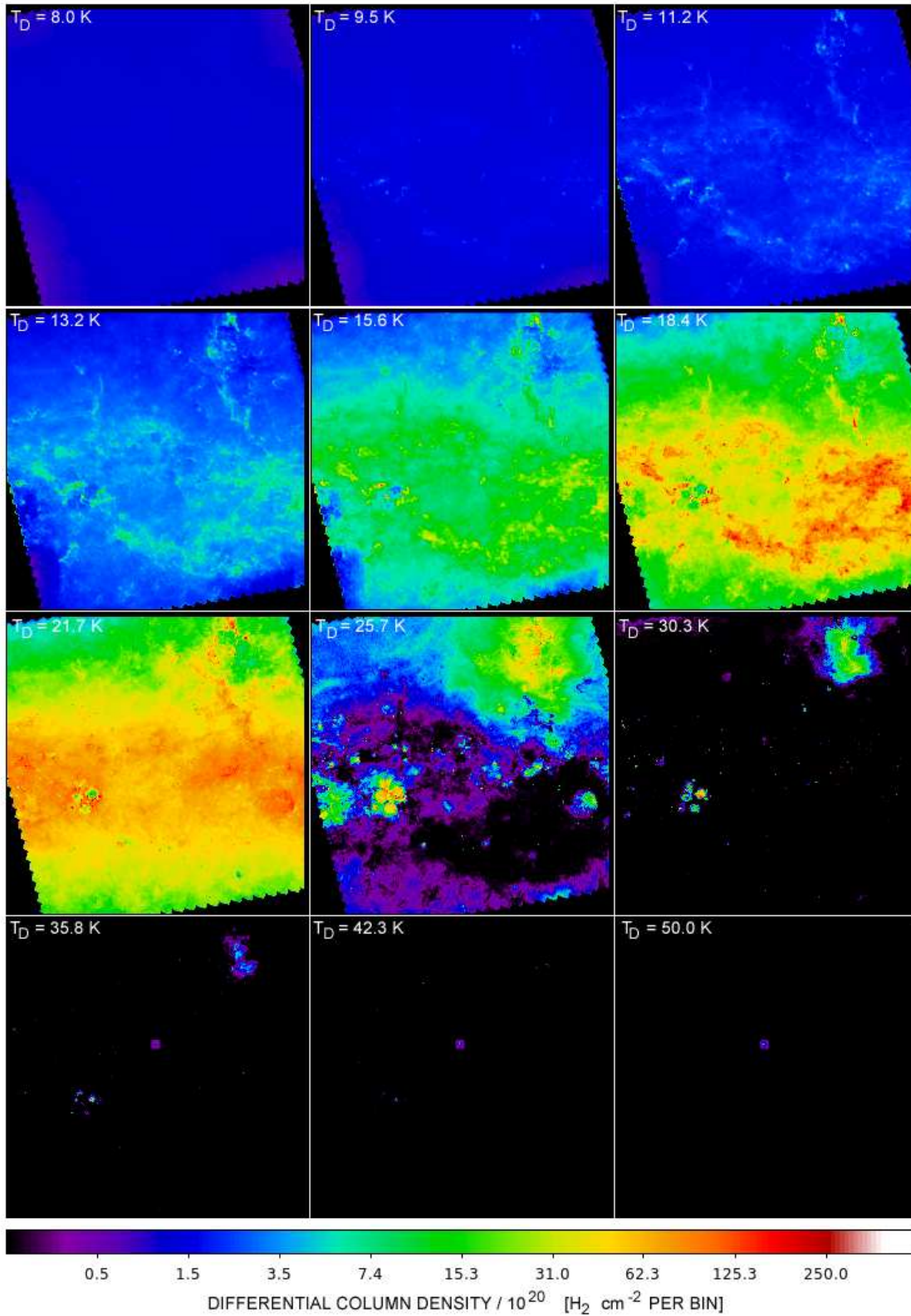
Figure 1. Maps of differential column density, generated by PPMAP, for the $2.4° \times 2.4°$ field of the Hi-GAL tile centred on Galactic longitude $\ell \simeq 17°$. The field contains the Eagle Nebula (M16), located in the upper right-hand quadrant. The corresponding dust temperature is specified at the top left of each panel—it represents the midpoint of a finite temperature interval or "bin" as defined in the text.
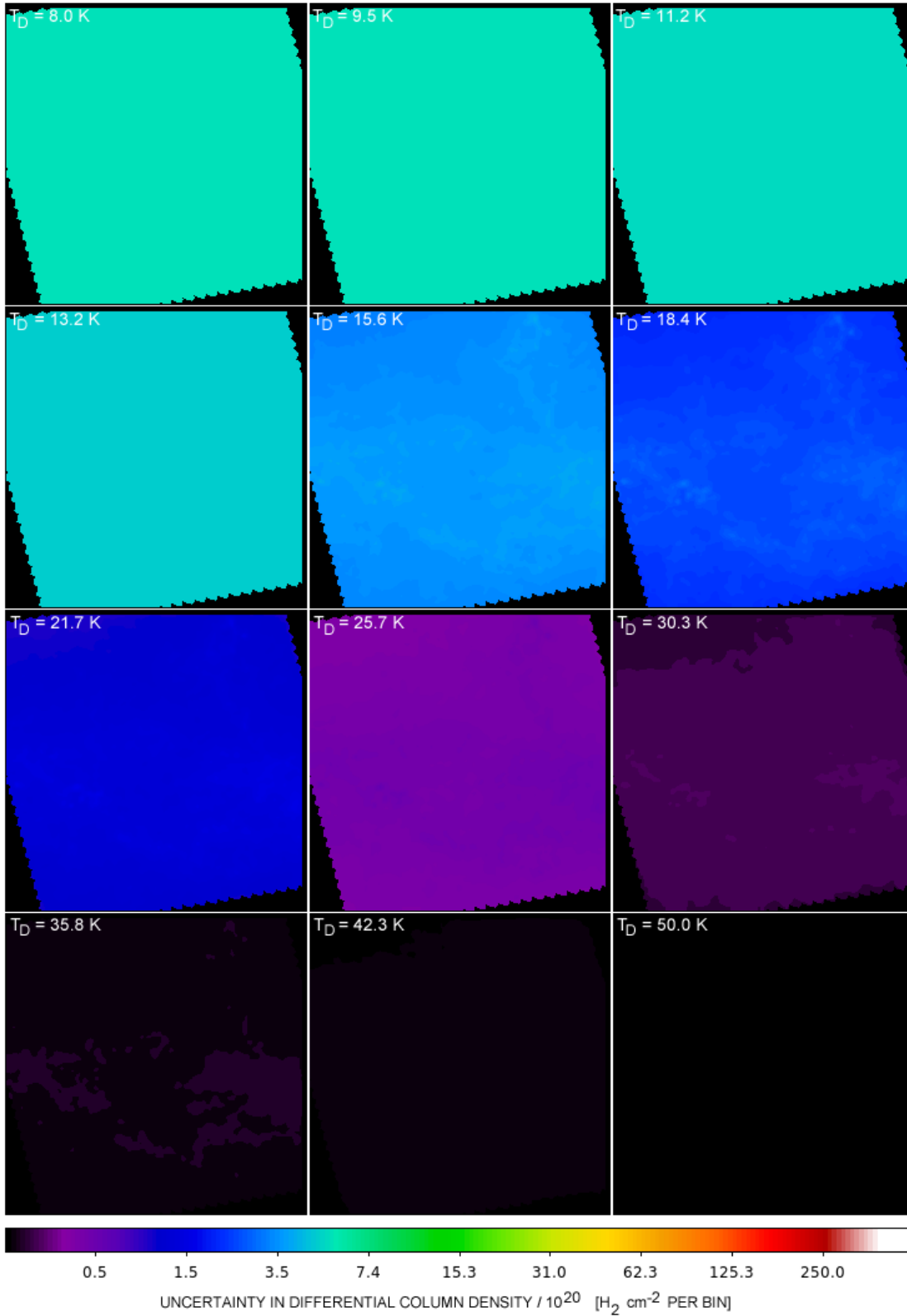
Figure 2. Uncertainty maps associated with the results shown in Fig. 1. Each represents the 1σ level of the corresponding map of differential column density.
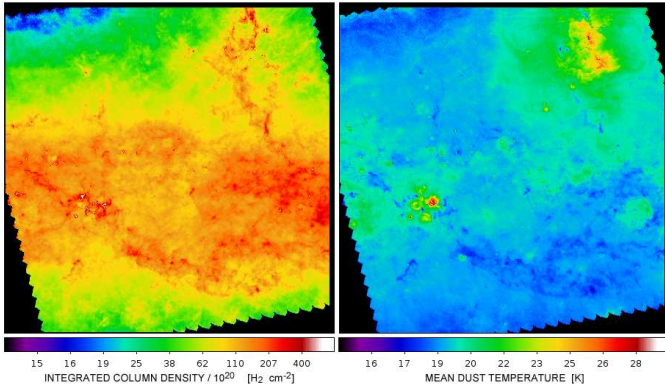
Figure 3. Maps of integrated column density and mean dust temperature for the $\ell \simeq 17°$ Hi-GAL tile, derived from the PPMAP image cube shown in Fig. 1. The peak column density is 5.3×10^{23} cm^{-2}, although the display scale is truncated at 8×10^{22} cm^{-2} to improve the visibility of low-level features.

Table 1. The effect of input parameter variations on the $\ell = 17°$ tile results.

$N_T{}^a$	β^b	η^c	$M_{\text{tot}}{}^d$ [$M_\odot$]	Peak col. dens. [H$_2$ cm^{-2}]	$\overline{T_{\text{D}}}{}^e$ [K]	$(T_{\text{D}})_{\min}$ [K]	$(T_{\text{D}})_{\max}$ [K]
12	2.0	10.0	1.1×10^6	5.3×10^{23}	19.6	13.0	42.3
8	2.0	10.0	1.1×10^6	5.2×10^{23}	19.4	13.8	40.2
12	1.5	10.0	1.1×10^6	4.4×10^{23}	20.6	12.4	40.0
12	2.0	0.3	1.4×10^6	4.4×10^{23}	18.6	12.7	37.3

[a] Number of values in the temperature grid between 10 K and 50 K.
[b] Opacity index.
[c] Dilution parameter.
[d] Total mass of dust+gas in the $2.4° \times 2.4°$ field.
[e] Density-weighted mean dust temperature along line-of-sight.

images. They represent spatially uncorrelated noise and do not include systematic effects such as flux calibration errors. The correlation of those errors between bands could, in principle, result in systematic effects in the variation of differential column density between temperature bins. However, simulations by Sadavoy et al. (2013) suggest that such correlations affect the estimated dust temperatures by less than 1 K. By far the largest source of uncertainty in the output maps arises from the assumed value of the reference opacity which may be in error by $\pm 50\%$.

The output uncertainty maps themselves represent the 1σ level of the random component of differential column density. Each pixel in these maps represents the *a posteriori* standard deviation of the corresponding pixel in the differential column density image. Examination of the map/uncertainty pairs shows that, in some cases, the differential column density maps contain apparently significant spatial structures which fall below the uncertainty level. This is due to the finite resolution along the temperature axis, which allows structure from one temperature plane to bleed through into an adjacent plane. As discussed by Marsh et al. (2015), increasing the number of observational wavelengths would increase the temperature resolution and hence reduce this tendency.

In order to investigate the sensitivity of PPMAP to variations in the input parameters, we have considered three cases in addition to the standard parameter set used to generate the results for the $\ell = 17°$ tile shown in Figs. 1–3, namely:

(i) changing the dust opacity index, β, to 1.5;
(ii) using fewer temperature bins, $N_T = 8$;
(iii) changing the dilution parameter, η, to 0.3.

For each parameter set we have compared the results for the $2.4° \times 2.4°$ field based on five metrics, namely the total cloud mass, peak column density, mean dust temperature, and the minimum and maximum dust temperatures over the field. The results are presented in Table 1, which shows that the estimates are not strongly perturbed by the input parameter variations. For example, the corresponding variations in estimated cloud mass and peak column density are at the $\sim 20\%$ level, while the temperature perturbations are

within the ± 1 K range corresponding to the typical temperature resolution expected for *Herschel* data based on the simulations conducted by Marsh et al. (2015).

We now discuss the results for two other regions in more detail, specifically the W5-E bubble and the filamentary complex in CMa OB1, and the radial variation of dust temperature in the Galaxy.

4.1 W5-E

The $\ell = 138°$ field is dominated by the Galactic HII region, W5-E, which forms part of the W5 bubble complex and is believed to be the site of triggered star formation (Deharveng et al. 2012). It is ionised by a central O star and exhibits morphological features characteristic of HII regions which have expanded into surrounding neutral material. These include bright-rimmed clouds, BRC13 and BRC14, and inwardly-directed pillars, discussed by Deharveng et al. (2012). Fig. 4 shows the differential column density image of the full $2.4° \times 2.4°$ tile in the dust temperature plane centred at $T_{\text{D}} = 21.7$ K.

Mapping of this field using the conventional[3] approach provides the images in panels (a) and (b) of Fig. 5, representing integrated column density and mean dust temperature. In that technique, the dust temperature is assumed to be constant along the line of sight and the data are first smoothed to a common spatial resolution. For comparison, panel (c) of Fig. 5 shows the results of applying the PPMAP technique to the same data. It is a composite image of W5-E showing the distribution of differential column density in three different dust temperature regimes, namely $T_{\text{D}} \leqslant 18.4$ K, $T_{\text{D}} = 21.7$ K, and $T_{\text{D}} \geqslant 25.6$ K. Overplotted on this figure are the locations of the bright-rimmed clouds, BRC13 and BRC14, and the two hot stars, HD 18326 and V1018 Cas.

Fig. 6 (lower portion) shows the PPMAP-derived differential column density in nine separate temperature planes spanning the range 9.5–35.8 K, for a small field of view

[3] For this example we have adopted the procedure and detailed parameters specified by Könyves et al. (2010), using images at all five *Herschel* continuum wavelengths, smoothed to 36 arcsec resolution, a pixel size of 6 arcsec, and a dust opacity law given by Eq. (1).
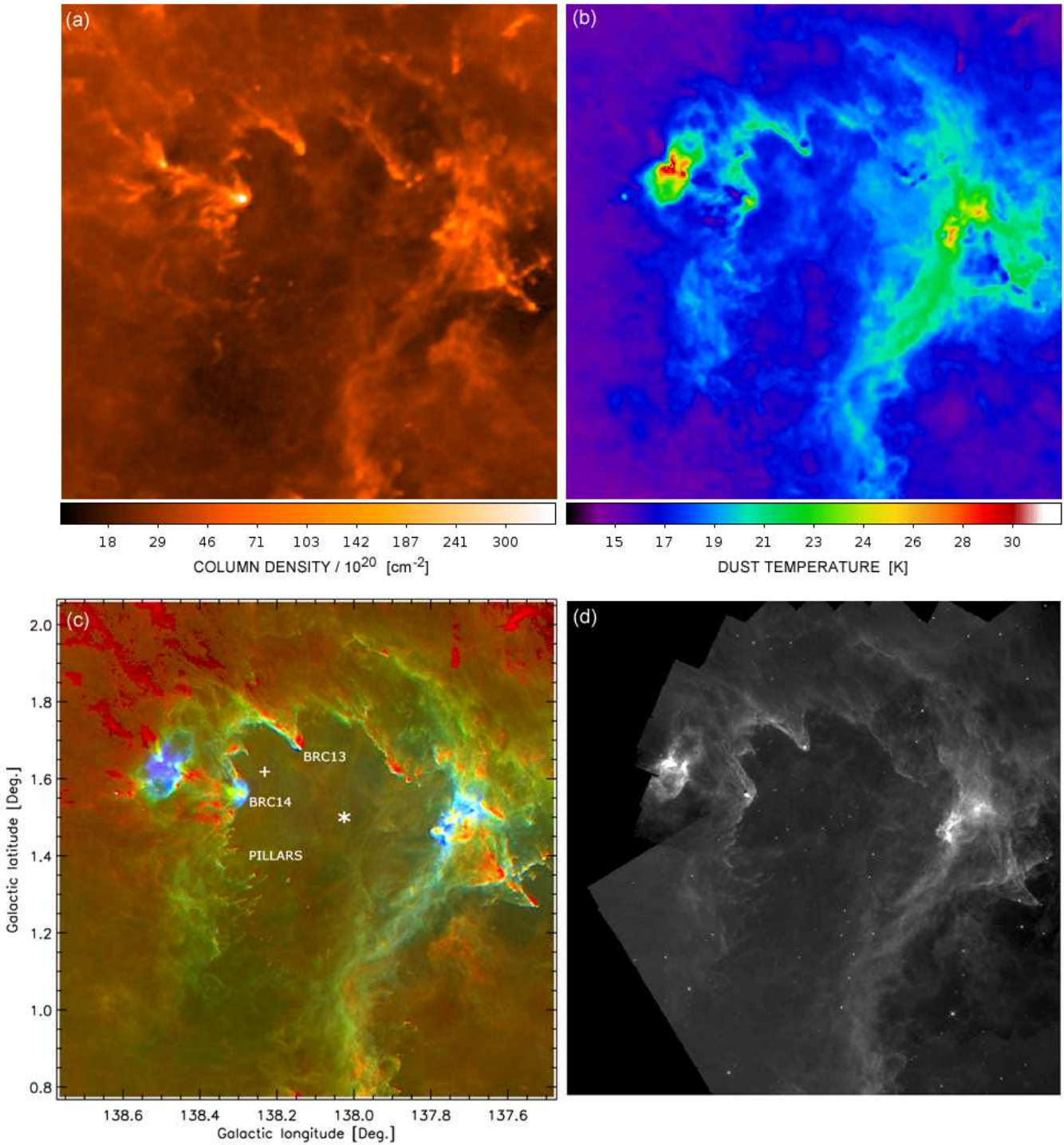
Figure 5. The W5-E HII region bubble. Panels (a) and (b) show the results obtained by the conventional column density mapping procedure (see text). Panel (c) shows the PPMAP results, represented as a composite map of differential column density in three different temperature regimes, namely $T_D \leqslant 18.4$ K (red), $T_D = 21.7$ K (green), and $T_D \geqslant 25.6$ K (blue). The ionising star HD 18326 (O7V) is indicated by the asterisk. Another hot star in the field is V1018 Cas (O7V–B1V), indicated by the "+" symbol. For comparison, (d) shows the 8 μm image from *Spitzer*.
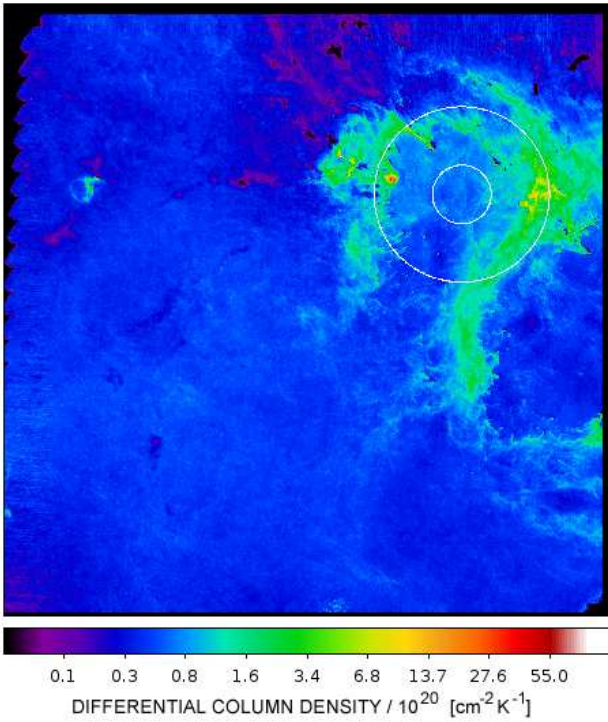
Figure 4. Differential column density, at a dust temperature of 21.7 K, over the $2.4° \times 2.4°$ field of the Hi-GAL tile centred at $\ell \simeq 138°$. The circles delineate subregions used in the calculation of the column density histograms shown in Fig. 10.

$(15' \times 15')$ around BRC13. It reveals that at the lowest temperatures ($T_{\rm D} \lesssim 11$ K) the only visible structure is a compact feature presumably representing a cool condensation at the tip of BRC13. Proceeding to higher temperatures, the column-like morphology of BRC13 becomes more apparent. For $T_{\rm D} \sim 11$–18 K a dark feature is visible along the eastern edge representing a deficit of material in that temperature range, but this edge becomes bright at $T_{\rm D} = 25.7$ indicating that hotter material has replaced cool material there. Moving to still higher temperatures we find that at $T_{\rm D} = 35.8$ K, the dust distribution is dominated by a warm compact structure at the southwestern tip of the column, suggesting a protostar which has formed in the condensation. It does, in fact, correspond with a young stellar object (YSO), of spectral class B5, whose ID is 16614 in the W5 IR Excess Spectral Catalog of Koenig & Allen (2011). For comparison, the upper portion of Fig. 6 shows the corresponding three-temperature composite extracted from Fig. 5, and also a pair of lower resolution maps (integrated column density and mean temperature) produced by the conventional mapping technique.

Some interesting features revealed by Figs. 5 and 6 are:

(i) the strong temperature gradient along the eastern edge of BRC13 which suggests heating from a direction other than the central O star. One possible heating source is the YSO at the tip of BRC14. Another is the hot star V1018 Cas. Although the latter is not regarded as a member of the W5 complex due to its ~ 40–50 km s^{-1} offset in radial velocity, it is conceivable that this offset could arise if the bubble complex were the result of a cloud-cloud collision via
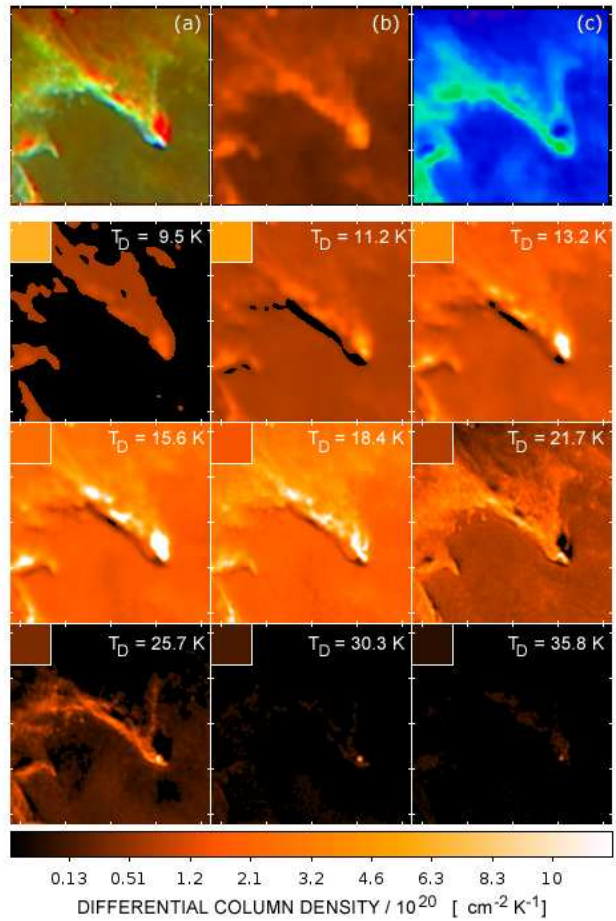

Figure 6. Zoom-ins of the BRC13 column in W5-E. *Upper row:* (a) Three-temperature composite produced by PPMAP, cut out from the bottom panel of Fig. 5; panels (b) & (c) show the results of the conventional mapping procedure in the form of integrated column density and mean dust temperature, respectively. *Lower 3×3 block:* Differential column-density, estimated by PPMAP, in nine different planes of dust temperature, $T_{\rm D}$, as indicated in the top right of each panel. In each case, the box in the top left indicates the 1σ uncertainty level. All panels are presented on the same scale of differential column density. The field of view in each case is $15' \times 15'$, centred on $(\ell, b) = (138.2052°, 1.7260°)$, and the pixel size is 6 arcsec (0.058 pc at the assumed 2 kpc distance). The tick marks are at intervals of 2 pc.

the model of Habe & Ohta (1992) in a similar fashion as for the RCW 120 bubble (Torii et al. 2015). Detailed radiative transfer modelling of BRC13, with constraints provided by the source luminosities and the estimated temperature gradient, may serve to identify the heating source and therefore potentially provide clues to the origin of the bubble complex;

(ii) the radially-directed "pillars" discussed by Deharveng et al. (2012), each of which has a cool condensation at its tip;

(iii) the morphology of the 22 K material (shown in green in panel (c) of Fig. 5) which has strong spatial correspondence with 8 μm emission imaged by *Spitzer*, shown in panel (d) of the same figure. That emission is believed to arise from PAH particles in the surrounding photodissociation region (PDR) which fluoresce in the ultraviolet radiation from the
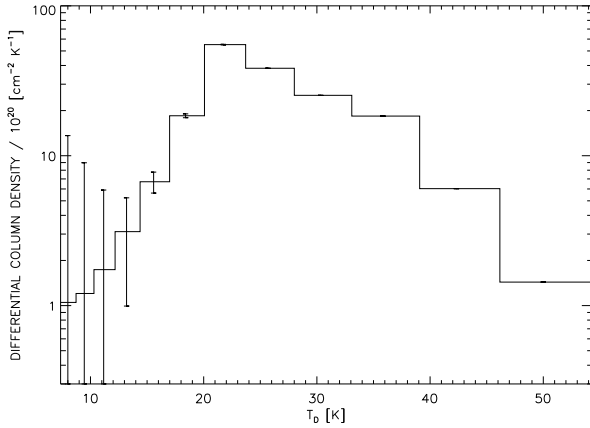
Figure 7. Profile of differential column density in W5-E as a function of dust temperature, at the location of the YSO at the tip of BRC14.

O star (Deharveng et al. 2012). This correspondence suggests that the PDR is characterised by dust at ∼ 22 K, enabling its spatial structure to be distinguished from that of other dust emission components along the line of sight.

The multiple-temperature planes of the ppmap image cube enable the temperature profile to be extracted at each spatial pixel location. An example is presented in Fig. 7 which shows the profile of differential column density as a function of temperature at the location of the YSO at the tip of BRC14. It shows that material at a range of dust temperatures between 15 K and 50 K coexists along the same line of sight, and hence the adoption of a single (mean) temperature is a very poor approximation.

Fig. 8 shows histograms of column density for portions of W5-E. Panel (a) is derived from pixels within a circular region of diameter 24 pc centred on the exciting star, corresponding to the bubble boundary as assessed by Deharveng et al. (2012). It is represented by the larger of the two circles overplotted in Fig. 4. Panel (b) is based on a smaller region corresponding to the interior circle in Fig. 4, representing lines of sight through the centre of the HII region rather than the peripheral structures. The reason that the blue histograms exceed the black (total) histograms at the low-density end is that, while the total column density includes contributions from warm low-density material, all lines of sight intersect higher density material somewhere along the way and thus the low density bins of the "total" histogram are unpopulated.

The histograms in (b) have a fairly simple interpretation in terms of a warm component whose column densities are distributed approximately as a lognormal, plus a cool component with a narrow range of column densities. The narrowness of this "spike" is probably the result of looking along the normal through the thin shell comprising the PDR. This indicates that some features in column density histograms can be the result of systematic effects related to geometry rather than representing purely the probability distribution of random density fluctuations related to turbulence. Interestingly, the spike occurs at the same column density as the peak of the broader distribution of cool dust in panel (a). This suggests the possibility that the broad apparent
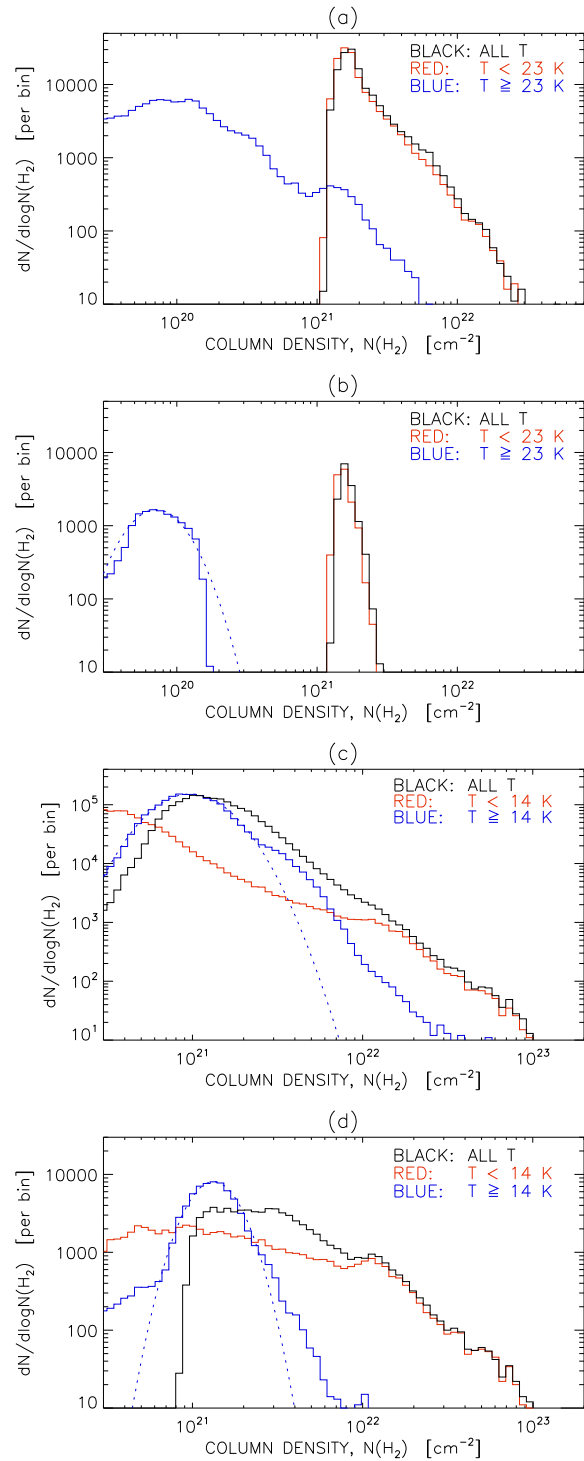

Figure 8. Column density histograms for W5-E and CMa OB1, as follows: (a) Overall bubble structure of W5-E; (b) Central part of W5-E. Details of the actual subregion boundaries are given in the text. Total column density is shown in black, while the coloured curves represent temperature ranges as indicated. (c) Full $2.4° \times 2.4°$ field containing CMa OB1; (d) Central filamentary complex in CMa OB1. The dotted lines represent least squares fits of lognormal functions to the histograms of the warm components. Note that, although the total of the black histogram values must equal the combined total for the red and blue histograms in each case, there is no requirement that the black histogram should equal or exceed the red or blue histogram at individual values of column density, as discussed further in the text.

power-law tail might be decomposed into separate narrow components of which the spike in (b) represents the low column density limit. Further analysis may thus shed light on whether the PDFs of star-forming clouds can be represented better by turbulence-induced lognormal distributions in the presence of noise (Brunt 2015), superpositions of lognormals from different parts of the field, combinations of lognormals and gravity-induced power-laws (Froebrich & Rowles 2010; Schneider et al. 2012, 2013), or truncated power laws (Lombardi et al. 2015). The distinction is important since it bears on the question of whether probability distribution functions (PDFs) of column density provide a probe of self-gravity effects in star-forming bubbles such as W5-E.

4.2   CMa OB1

The $\ell = 224°$ tile is dominated by the large filamentary complex of CMa OB1, a site of prolific star formation (Elia et al. 2013). The spatial distribution of temperature-differential column density at $T_D = 13.2$ K, produced by PPMAP, is shown in Fig. 9. Maps of integrated column density and density-weighted mean dust temperature for a $20' \times 20'$ sub-region are shown in Fig. 10 (panels a and c, respectively). Panels (b) and (d) enable a comparison with the results of the "conventional" technique discussed earlier. Specifically panel (b) shows the ratio of estimated column densities (PPMAP divided by "conventional"), while panel (d) represents the temperature *difference* (PPMAP minus "conventional"). While the two techniques give comparable results for large areas of the background, PPMAP gives larger estimates of column density at the peaks of compact sources (by factors of up to 6). It also gives lower estimated temperatures in cool compact sources (cores) and larger peak values for the warm compact sources (protostars). These differences result partly from the increased spatial resolution provided by deconvolution, and also from the increased accuracy obtained by dispensing with the uniform temperature assumption. Interestingly, the PPMAP estimate of total mass within the $20' \times 20'$ region (4700 $M_\odot$) is significantly smaller (by a factor of 0.6) than the value 7700 $M_\odot$ yielded by the "conventional" method. The apparent discrepancy results from relatively small differences in mean dust temperature (13.7 K and 13.0 K) as estimated by the two techniques, respectively.

The full image cube for the main part of the filamentary complex has been presented by Marsh et al. (2015). It enabled the PDF of column density to be decomposed by temperature, showing the warm ($T_D > 13$ K) and cool ($T_D < 13$ K) material to be characterised by different distributions of column density. Specifically, the PDF of the warm material was found to be well approximated by a lognormal, as expected for density fluctuations resulting from interstellar turbulence, while that of the cool material was consistent with power law behaviour due to the effects of self-gravity on those fluctuations (Klessen 2001; Kainulainen et al. 2009; Kritsuk, Norman & Wagner 2011; Schneider et al. 2013; Girichidis et al. 2014).

The lower two panels of Fig. 8 show column density histograms, representing estimates of PDFs, derived for the $\ell = 224°$ tile using PPMAP. Panel (c) is for the full $2.4° \times 2.4°$ field, while panel (d) is for a more limited region enclosing the main part of the filamentary complex as indicated by
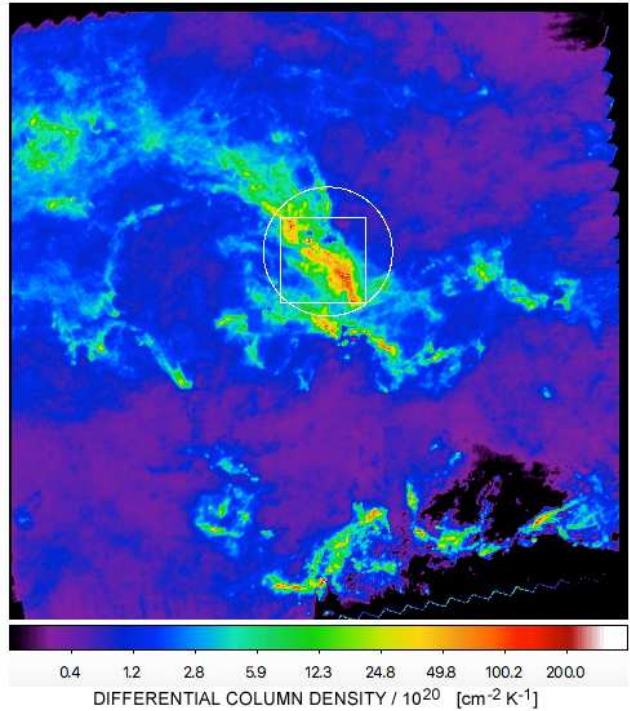

DIFFERENTIAL COLUMN DENSITY / 10^{20} [cm^{-2} K^{-1}]

Figure 9. Differential column density, at a dust temperature of 13.2 K, over the $2.4° \times 2.4°$ field of the Hi-GAL tile at $\ell \simeq 224°$. The circle delineates a subregion used in the calculation of column density histograms shown in Fig. 8. The square represents the boundary of the cutout region shown in Fig. 10.

the circular boundary in Fig. 8. The histograms of total column density (shown in black) have been decomposed into contributions from warm ($T_D \geqslant 14$ K) and cool ($T_D < 14$ K) material, represented by the blue and red histograms, respectively. Clearly, the warm material exhibits lognormal-like behaviour while the cool material accounts for the high density tail. The separate histograms for the smaller subregion illustrate the effect of field selection on the shape of the histogram. The circular boundary in this case is intended to delineate the region which appears to contain the majority of star formation activity, based largely on visual inspection. An interesting line of research to be pursued in the future is to explore how the PDFs of temperature-differential column density vary between different subregions and between concentric regions of different size, as has been done previously with PDFs of *total* column density (Russeil et al. 2013; Tremblin et al. 2014; Schneider et al. 2015a,b).

4.3   Radial profile of dust temperature in the Galaxy

Estimates of dust temperature can provide strong constraints on the interstellar radiation field (ISRF), which is of interest not only for star formation models, but also for the propagation of cosmic rays in the Galaxy (Porter & Strong 2005). In a previous study, Sodroski et al. (1997) used data from the DIRBE instrument on *COBE*, in combination with ^{12}CO, HI, and radio continuum data, to estimate the dust temperature as a function of Galactocentric distance for the dust embedded in neutral atomic (HI), molecular (H$_2$), and
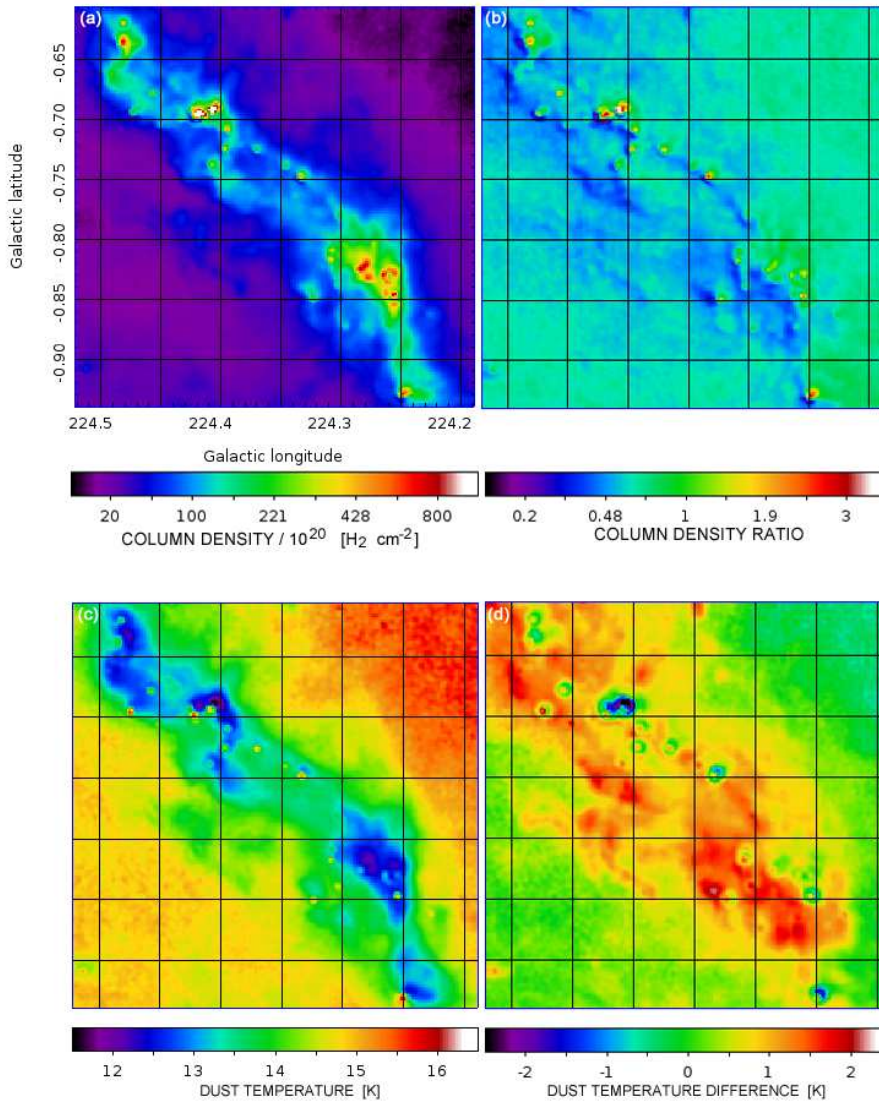
Figure 10. Comparison between results of PPMAP and the "conventional" column density mapping technique (see text) for a $20' \times 20'$ subfield of the $\ell \simeq 224°$ Hi-GAL tile (delineated by the square region in Fig. 9), showing part of the CMa OB1 filamentary complex. (a) Integrated column density from PPMAP; (b) column density ratio (PPMAP divided by "conventional"); (c) mean dust temperature; (d) dust temperature difference (PPMAP minus "conventional").

ionised (HII) hydrogen. In all cases they found that the dust temperature decreases with radial distance, but with large error bars and relatively low spatial resolution.

Here we report the first *Herschel*-based estimate of the radial profile of dust temperature in the Galactic Plane. This is accomplished by first calculating the mean dust temperature (weighted by differential column density) using the image cube generated by PPMAP for each $2° \times 2°$ Hi-GAL tile. Then, in order to assign a characteristic heliocentric distance to each tile, a Galactic spiral arm model is needed. We base our heliocentric distances on the results presented by Reid et al. (2016), which make use of trigonometric parallaxes from VLBI observations of water and methanol masers in high mass star formation regions, supplemented with other data such as kinematic information from CO observations. Where necessary, ambiguities in spiral arm identification are resolved with the aid of the peaks in source counts associ-

ated with tangential directions, in a fashion similar to that discussed by Ragan et al. (2016). The heliocentric distances are then converted to Galactocentric distances assuming a distance to the Galactic centre of 8.4 kpc (Reid et al. 2009).

The top panel of Fig. 11 shows a plot of mean dust temperature as a function of Galactocentric distance. It exhibits a clear trend of decreasing dust temperature with increasing distance. To check whether this trend could be an artifact due to differing *heliocentric* distances, Fig. 12 shows the corresponding plot as a function of heliocentric distance instead. The lack of correlation indicates that the estimated dust temperatures depend on Galactocentric rather than heliocentric distance. We note also that our *Herschel*-based estimates are reasonably consistent with those of Sodroski et al. (1997) which are shown overplotted on Fig. 11.

The image cubes serve to characterise not just the mean dust temperature, $\overline{T_D}$, but also higher order moments of
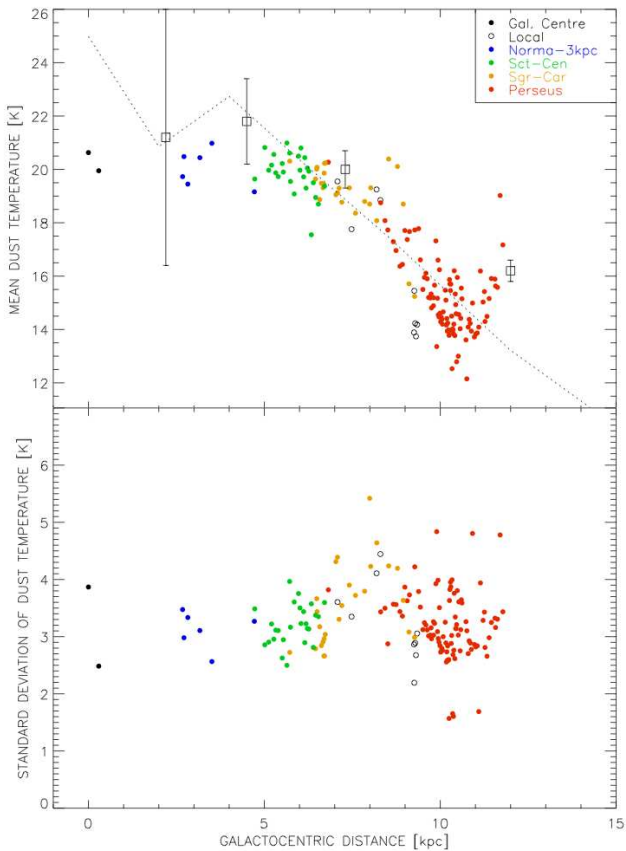
Figure 11. *Upper panel:* mean dust temperature as a function of Galactocentric distance. The colour coding represents the assumed spiral arm indentifications based on the results presented by Reid et al. (2016), as indicated in the upper right of the panel. The dotted line represents the model curve based on the ISRF of Porter et al. (2008). The open squares with error bars are from Sodroski et al. (1997). *Lower panel:* the standard deviation of dust temperature values (along the line of sight as well as in the plane of the sky) as a function of Galactocentric distance.
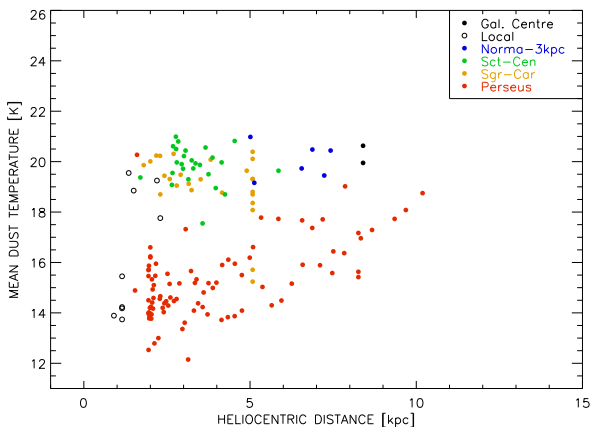

Figure 12. Mean dust temperature as a function of heliocentric distance, to be compared with the variation with respect to *Galacto*centric distance shown in Fig. 11.

dust temperature along the line of sight. The lower panel of Fig. 11 shows the standard deviation of dust temperature values within the image cube for each Galactocentric distance. The median value is 3.2 K, and there is no significant trend with Galactocentric distance. Similarly, we find no pronounced trends with Galactocentric distance for the normalised skewness and kurtosis, for which the median values are -0.3 and 3.5, respectively. Those quantities are defined as the density-weighted mean values of $(T_{\rm D} - \overline{T_{\rm D}})^3$ and $(T_{\rm D} - \overline{T_{\rm D}})^4$, divided by the variance to the power of $3/2$ and 2, respectively; their theoretical values for a pure Gaussian distribution are 0 and 3.0, respectively. The PPMAP results thus serve to characterise the overall temperature variation in the Galactic plane as essentially a Gaussian with constant variance such that the only significant variation with Galactocentric distance is in the mean value.

It is of interest to ask whether the observed variation of mean dust temperature with radial distance, r, is consistent with heating by the ISRF. We can compare our estimates in Fig. 11 with a model prediction by noting that, based on the ISRF heating model, the dust temperature $T_{\rm D}(r)$ should vary as $I_{\rm ISRF}(r)^{\frac{1}{4+\beta}}$, where β is the dust opacity index (Bernard et al. 2010) and $I_{\rm ISRF}(r)$ is the bolometric intensity of the ISRF. Assuming $\beta = 2$, using the wavelength-integrated ISRF intensities from Porter et al. (2008)[4] and the *COBE* measurement of mean dust temperature in the solar neighbourhood, 17.5 K (Lagache et al. 1998), we obtain the model curve represented by the dotted line in Fig. 11. The model curve is largely consistent with the distribution obtained from the Hi-GAL data, and with the previous observational estimates from Sodroski et al. (1997), but there are some qualitative differences as discussed below.

5   DISCUSSION

These results serve to illustrate the information which can be gained from the line-of-sight temperature decomposition provided by PPMAP in the study of dusty Galactic structures on all scales. The main assumption involved is that the dust emission is optically thin. This is valid over most of the Galactic Plane at the *Herschel* wavelengths—the fraction of output pixels for which the inferred optical depth exceeds unity is $\sim 10^{-4}$ at 70 μm and $\sim 10^{-6}$ at 160 μm. Thus violations of the optically thin assumption have negligible effect on estimates of the large-scale variation of dust temperature in the Galaxy. There are, however, localised regions of high 70 μm optical depth in dense molecular clouds, and one might expect an impact on estimates of peak column density and core masses. However, a study of the dense molecular cloud 'The Brick' by Marsh et al. (2016) suggests that high optical depth at a single wavelength (70 μm) does not significantly perturb the solution provided there is sufficient signal to noise at the longer wavelengths. Nevertheless, we cannot discount the possibility that there exist some very dense cores for which optical depth effects would result in underestimates of column density and hence core mass.

We find that for the star-forming HII region/bubble,

W5-E, the temperature decomposition facilitates the separation of distinct physical components which would normally be superposed along the line of sight in conventional mapping. One example is the image of 22 K dust which apparently represents the morphology of the PDR surrounding the HII region, whereas images at lower temperatures are dominated by cooler core-forming material and those at higher temperatures are dominated by features which represent protostars and possibly a bow shock. All of these phenomena co-exist along some of the same lines of sight but are separable in different temperature planes. In a similar fashion, the temperature-dependent images of differential column density in CMa OB1 provide separate views of the cool filamentary material and the warmer overlying material of the ISM. The W5-E results also reveal the existence of a strong temperature gradient along one edge of a column-like protrusion which requires a heating source other than the ionising star. If subsequent radiative transfer modelling reveals that source to be the O7/B1 star V1018 Cas, it would strongly suggest the latter to be a member of the W5-E complex despite its large offset in radial velocity. This might be due to W5-E having been formed in a cloud-cloud collision (e.g., Habe & Ohta 1992) or it might be the result of a dynamical sling-shot ejection. The ubiquitousness of such bubbles in the Galactic plane (see, for example, Anderson et al. 2011) means that the set of ppmap image cubes from Hi-GAL should provide a large enough statistical sample to draw some more general conclusions regarding the possible role of phenomena such as cloud-cloud collisions in the formation of these objects (e.g., Balfour et al. 2015).

Although our estimated radial variation of dust temperature in the Galaxy can be explained broadly in terms of heating of the dust grains by the ISRF, not all features are reproduced by the simple heating model. The estimated variation, in fact, appears to be characterised by two regimes, one in which the temperature is approximately constant out to ~ 6 kpc, and the other which exhibits a relatively steep falloff beyond that. The transition point appears to coincide with the sudden increase in the proportion of molecular with respect to neutral hydrogen in the inner Galaxy (Sodroski et al. 1997), and might therefore be understood in terms of the shielding effects of dust in dense molecular clouds.

The Sodroski et al. (1997) results suggest that for most of the range in radial distance, the dust component dominating our temperature estimates is located in the diffuse HI clouds of the Galaxy. In a forthcoming paper we will use information gathered from compact source extractions to help distinguish between the Galactic temperature profiles of the diffuse cloud component and the denser star-forming clouds. We will also investigate possible connections with radial trends in star formation rate (see, for example, Ragan et al. 2016).

6 CONCLUSIONS

The ppmap technique provides image cubes of differential column density as a function of dust temperature and (x, y) sky location and represents a clear advance in our ability to extract information on dust distributions from continuum observations at multiple wavelengths. It thus represents an important tool within the vialactea project for the analysis of Hi-GAL data in conjunction with supplementary data at other wavelengths where available. Specific advantages are:

(i) increased spatial resolution resulting from the incorporation of PSF knowledge; all observational images are used at their native resolution and it is not necessary to smooth to a common resolution;

(ii) increased accuracy of peak column densities of compact features, due both to the resolution improvement and to taking proper account of temperature variations along the line of sight;

(iii) the temperature decomposition provides the potential ability to distinguish different physical phenomena superposed along the line of sight, as discussed above.

We have processed all 163 tiles of the Hi-GAL survey, each of which covers a $\sim 2° \times 2°$ region of the Galactic plane. The results, now publicly available online, consist of:

(i) a total of 163 image cubes of differential column density with 6 arcsec spatial pixels and 12 values along the temperature axis, covering the range 8–50 K in dust temperature;

(ii) corresponding image cubes of the uncertainties;

(iii) 2D maps of total column density and density-weighted mean dust temperature, derived from the image cubes.

In this paper we have presented some examples of analyses that can be carried out with these data, focussing on the HII region bubble W5-E, a star-forming filamentary complex in CMa OB1, and the radial distribution of dust temperature in the Galaxy. In W5-E we have identified a strong temperature gradient in a pillar-like feature which may have implications for models of the bubble formation. For CMa OB1 we confirm our previous findings regarding the temperature dependence of the form of the PDF of differential column density, and also find evidence for spatial variations of that quantity within the same star formation region. Finally, we find that the radial dust temperature profile of the Galaxy shows a monotonic decrease from the centre in rough agreement with published models of the interstellar radiation field, but that it also exhibits a prominent central plateau which is not predicted by such models and which therefore merits further investigation.

REFERENCES

Anderson, L. D., Bania, T. M., Balser, D. S., & Rood, R. T. 2011, ApJS, 194, 32

Balfour, S. K., Whitworth, A. P., Hubber, D. A., & Jaffa, S. E. 2015, MNRAS, 453, 2471

Bernard, J.-Ph., Paradis, D., Marshall, D. J. et al. 2010, A&A, 518, L88

Brunt, C. M. 2015, MNRAS, 449, 4465

Cambresy, L., Boulanger, F., Lagache, G., & Stepnik, B. 2001, A&A, 375, 999

Deharveng, L., Zavagno, A., Anderson, L. D. et al. 2012, A&A, 546, A74

Elia, D., Molinari, S., Fukui, Y. et al. 2013, ApJ, 772, 45

Froebrich, D. & Rowles, J. 2010, MNRAS, 406, 1350

Girichidis, P., Konstandin, L., Whitworth, A. P. & Klessen, R. S. 2014, ApJ, 781, 91

Griffin, M. J., North, C. E., Amaral-Rogers, A. et al. 2013, MNRAS, 434, 992

Hester, J. J., Scowen, P. A, Sankrit, R. et al. 1996, AJ, 111, 2349

Hildebrand, R. H. 1983, QJRAS, 24, 267

Hill, T., Motte, F., Didelon, P. et al. 2012, A&A, 542, A114

Kainulainen, J., Beuther, H., Henning, T. & Plume, R. 2009, A&A, 508, L35

Koenig, X. P. & Allen, L. E. 2011, ApJ, 726, 18

Klessen, R. S. 2001, ApJ, 556, 837

Könyves, V., André, Ph., Men'shchikov, A. et al. 2010, A&A, 518, L106

Kritsuk, A. G., Norman, M. L. & Wagner, R. 2011, ApJ, 727, L20

Lagache, G, Abergel, A., Boulanger, F., & Puget, J.-L. 1998, A&A, 333,709

Lombardi, M., Alves, J., & Lada, C. J. 2015, A&A, 576, L1

Marsh, K. A., Whitworth, A. P. & Lomax, O. 2015, MN-RAS, 454, 4282

Marsh, K. A., Ragan, S. E., Whitworth, A. P. & Clark, P. C., 2016, MNRAS, 461, 16

Habe, A. & Ohta, K. 1992, PASJ, 44, 203

Molinari, S., Swinyard, B., Bally, J., et al. 2010, PASP, 122, 314

Molinari, S., Bally, J., Glover, S. et al. 2014, in Protostars and Planets VI, Henrik Beuther et al. eds., University of Arizona Press, Tucson, 914, 125

Ott, S. 2010, in ASP Conf. Ser. 434, Astonomical Data Analysis Software and Systems XIX, ed. Y Mizumoto, K.-I. Morita, & M. Ohishi (San Francisco, CA; ASP), 139

Palmeirim, P., André, Ph., Kirk, J. et al. 2013, A&A, 550, A38

Paradis, D., Bernard, J.-P., Mény, C., & Gromov, V. 2011, A&A, 534, 118

Peretto, N., Fuller, G. A., Plume, R. et al. 2010, A&A, 518, 98

Pezzuto, S. 2013, HERSCHEL Document Ref.: PICC-CR-TN-044

Piazzo, L., Calzoletti, F., Faustini, M. et al. 2015 MNRAS, 447, 1471

Pilbratt, G. L., Riedinger, J. R., Passvogel, T., et al. 2010, A&A, 518, L1

Poglitsch, A., Waelkens, C., Geis, N., et al. 2010, A&A, 518, L2

Porter, T. A. & Strong, A. W. 2005, 29th International Cosmic Ray Conference Pune, 4, 77

Porter, T. A., Moskalenko, I. V., Strong, A. W. et al. 2008, ApJ, 682, 400

Ragan, S. E., Moore, T. J. T., Eden, D. J. et al. 2016, MNRAS, 462, 3123

Rathborne, J. M., Longmore, S. N., Jackson, J. M. et al. 2015, ApJ, 802, 125

Reid, M. J., Menten, K. M., Zheng, X. W. et al. 2009, ApJ, 700, 137

Reid, M. J., Dame, T. M.,, Menten & K. M., Brunthaler, A. et al. 2016, ApJ, 823, 77

Russeil, D., Schneider, N., Anderson, L. D. et al. 2013, A&A, 554, 42

Sadavoy, S. I., Di Francesco, J., André, Ph. et al.. 2012, A&A, 540, A10

Sadavoy, S. I., Di Francesco, J., Jonhstone, D. 2013, ApJ, 767, 126

Schneider, N., Csengeri, T., Hennemann, M. et al. 2012, A&A, 540, 11

Schneider, N., André, Ph., Könyves, V. et al. 2013, ApJ, 766, L17

Schneider, N., Ossenkopf, V., Csengeri, T. et al. 2015a, A&A, 575, 79

Schneider, N., Csengeri, T., Klessen, R. S. et al. 2015b, A&A, 578, 29

Sodroski, T. J., Odegard, N., Arendt, R. G. et al. 1997, ApJ, 480, 173

Torii, K., Hasegawa, K., Hattori, Y. et al. 2015, ApJ, 806, 7

Tremblin, P., Anderson, L. D., Didelon, P. et al. 2014, A&A, 568, 4

Valtchanov, I. 2014, HERSCHEL-DOC-0798, version 2.5, March 24, 2014

This paper has been typeset from a TEX/ LATEX file prepared by the author.